

Reconstructing Three-dimensional Structure of Underlying Triaxial Dark Halos From X-ray and Sunyaev–Zel’dovich Effect Observations of Galaxy Clusters

JOUNGHUN LEE AND YASUSHI SUTO

Department of Physics, The University of Tokyo, Tokyo 113-0033, Japan

`lee@utap.phys.s.u-tokyo.ac.jp, suto@phys.s.u-tokyo.ac.jp`

ABSTRACT

While the use of galaxy clusters as *tools* to probe cosmology is established, their conventional description still relies on the spherical and/or isothermal models that were proposed more than 20 years ago. We develop, instead, a deprojection method to extract their intrinsic properties from X-ray and Sunyaev–Zel’dovich effect observations in order to improve our understanding of cluster physics. Assuming that the underlying gravitational potentials are well approximated by those of triaxial dark halos with a constant axis ratio, we provide several accurate empirical fitting formulae for the gas density and temperature profiles, and for the projected surface brightness relevant to X-ray and Sunyaev–Zel’dovich effect observations. Those models allow us to reproduce the 3D structure of the underlying dark halos from those projected profiles.

Subject headings: cosmology:theory – dark matter – galaxies: clusters: general

1. INTRODUCTION

Understanding of statistical properties of *dark matter halos* has been significantly advanced in recent years, largely from high-resolution numerical simulations (Navarro, Frenk, & White 1996, 1997; Fukushige & Makino 1997; Moore *et al.* 1998; Jing & Suto 2000, 2002). Given those theoretical/empirical successes, a next natural question is how to apply them for the description of *real* galaxy clusters. While there exist a number of attempts along this line, they usually assume the spherical symmetry of the underlying halos (Makino, Sasaki & Suto 1998; Suto, Sasaki & Makino 1998; Yoshikawa & Suto 1999). This paper describes a methodology to reconstruct the three-dimensional (3D) structure of dark halos from the two-dimensional (2D) surface brightness profiles of intra-cluster gas from the X-ray and Sunyaev-Zel’dovich (SZ) effect observations assuming that the halos are triaxial ellipsoids.

Indeed it is a classical problem in astrophysics to determine the 3D properties of astronomical objects from the observed 2D counterparts (e.g., Lucy 1974; Fabricant et al. 1984; Dehnen & Gerhard 1993; Binney, Davies, & Illingworth 1990; Gerhard & Binney 1996). A primary example is that of deprojecting galaxy clusters. Fabricant et al. (1984) analyzed the X-ray surface brightness map, and showed that the cluster mass distribution is far from spherical. Zaroubi et al. (1998) developed a general method of deprojecting the 2D images of rich clusters based on the Fourier slice theorem to reconstruct a 3D cluster structure. Later their technique was applied and tested against the numerically simulated galaxy clusters (Zaroubi et al. 2001). Yoshikawa & Suto (1999) proposed a deprojection method for spherical clusters based on the Abel integral. Reblinsky (2000) provided a parameter-free Richardson-Lucy algorithm to reconstruct the 3D gravitational potential, and demonstrated its stability by applying to gas-dynamical simulations. Dore et al. (2001) provided a perturbative approach to the cluster deprojection, taking into account the non-isothermality and asphericity of galaxy clusters. Recently, Fox & Pen (2002) also considered the problem of deprojecting the aspherical clusters. They first constructed a parameterized 3D aspherical model of galaxy clusters, and found the 3D cluster shape by determining the best-fit parameters through χ^2 -fitting between the model predictions and the observational data.

All the previous approaches, however, were based on the rather restricted assumptions of axial symmetry (oblate or prolate) and/or isothermality of galaxy clusters. Furthermore they usually require combining X-ray and/or SZ effect data with weak lensing (WL) map, which significantly limits the applicability of those approaches. Our goal here is to find a more general method of cluster deprojection that is free from the assumptions of axial symmetry, gas isothermality or the angles between the line-of-sight direction and the cluster principal axes.

Lee & Suto (2003; hereafter Paper I) obtained an analytical approximation to the intra-cluster gas profiles on the basis of perturbation theory assuming that the underlying dark halos are triaxial. Here, instead of the perturbative analytic approximation, we provide a series of accurate empirical fitting formulae for the 2D and 3D profiles of intra-cluster gas embedded in triaxial dark halos that is independent of the degree of the cluster asphericity. Then we develop a general cluster deprojection method based on the fitting formulae that can be applied to triaxial clusters with the surface brightness map in X-ray or radio bands without requiring the WL information.

The organization of this paper is as follows. In §2 we provide a series of empirical fitting formulae for the density profiles of the intra-cluster gas in hydrostatic equilibrium in the triaxial dark halos. In §3 we study the deprojection effect of the 3D gas profiles on the plane of the sky, and provide another series of empirical fitting formula for the 2D surface

brightness density profiles. In §4 we present an algorithm to reconstruct the 3D structures of the underlying dark halos from the observed 2D cluster profiles, and test it against the numerical realizations. Finally we discuss the results and summarize our conclusions in §5.

2. MODELING INTRA-CLUSTER GAS PROFILES

2.1. Gravitational Potential of Dark Matter Halos

To predict theoretically the X-ray and SZ profiles of galaxy clusters, one first needs a good physical model for the intra-cluster gas. Here we assume that the intra-cluster gas is either isothermal or polytropic, and in hydrostatic equilibrium within the gravitational potential generated by a concentric and coaxial triaxial dark matter halo.

Consider a triaxial dark halo whose iso-density surfaces are given by the following equation:

$$R^2 \equiv x^2 + \frac{y^2}{1 - e_b^2} + \frac{z^2}{1 - e_c^2}, \quad (1)$$

where the Cartesian system of coordinates (x, y, z) is aligned with the halo principal axes, oriented such that the x -axis and z -axis runs lies along the major and minor principal axes respectively. R is the major axis length of the iso-density surface, and e_b and e_c ($e_b < e_c$) represent the two constant eccentricities of the ellipsoidal dark halos. Equation (1) implies that the density profile of a triaxial dark matter halo should be a function of the major axis length R .

We adopt the density profile of triaxial dark halos proposed by Jing & Suto (2002):

$$\rho(R) = \frac{\delta_c \rho_{\text{crit}}}{(R/R_0)^\alpha (1 + R/R_0)^{3-\alpha}}, \quad (2)$$

where R_0 is the scale length, δ_c is the dimensionless characteristic density contrast with respect to the critical density ρ_{crit} of the universe at the present epoch, and α represents the inner slope of the density profile. Jing & Suto (2002) showed that $\alpha \approx 1$ on the cluster scale and $\alpha \approx 3/2$ on the galaxy scale. For simplicity and definiteness, we focus on the case of $\alpha = 1$ throughout this paper.

The gravitational potential due to the ellipsoidal bodies described by equation (2) is formally expressed as (Binney & Tremaine 1987):

$$\Phi(\mathbf{r}) = -\pi G \sqrt{(1 - e_b^2)(1 - e_c^2)} \int_0^\infty \frac{[\psi(\infty) - \psi(m)]}{\sqrt{(\tau + 1)(\tau + 1 - e_b^2)(\tau + 1 - e_c^2)}} d\tau, \quad (3)$$

$$\psi(m) = 2 \int_0^m \rho(R) R dR, \quad m^2 = \frac{x^2}{\tau + 1} + \frac{y^2}{\tau + 1 - e_b^2} + \frac{z^2}{\tau + 1 - e_c^2}. \quad (4)$$

Equations (3) and (4) along with equation (2) allows one to compute the triaxial halo gravitational potential at least numerically. Note that while the halo gravitational potential $\Phi(\mathbf{r})$ depends not only on e_b , e_c and α but also on δ_c , ρ_{crit} , and R_0 , the dependence on the latter sets of parameters can be factored out. Thus we introduce a dimensionless potential $\tilde{\Phi}$ that depends only on e_b , e_c and α :

$$\Phi(\mathbf{r}; e_b, e_c, \alpha, \delta_c, \rho_{\text{crit}}, R_0) = 4\pi G \delta_c \rho_{\text{crit}} R_0^2 \tilde{\Phi}(\mathbf{r}; e_b, e_c, \alpha). \quad (5)$$

2.2. Gas Density and Temperature Profiles in terms of the Halo Gravitational Potential

To determine the intra-cluster gas profiles in terms of the underlying halo potential, one needs to specify the equation of state for the intra-cluster gas. We consider both the isothermal and the polytropic cases in order.

2.2.1. Isothermal gas

The equation of state for the isothermal gas is given as

$$P_g(\mathbf{r}) = P_{g0} [\rho_g(\mathbf{r})/\rho_{g0}], \quad (6)$$

where P_g and ρ_g represent the gas pressure and the gas density, respectively. In what follows, the subscript 0 of some physical variable indicates the value of that physical variable at the center $\mathbf{r} = 0$.

Now the density profile of the isothermal gas in hydrostatic equilibrium is derived as

$$\rho_g(\mathbf{r}) = \rho_{g0} \exp \left[-\kappa \{ \tilde{\Phi}(\mathbf{r}) - \tilde{\Phi}_0 \} \right]. \quad (7)$$

We define a dimensionless isothermal gas constant κ as

$$\kappa \equiv \frac{4\pi G m_p \mu_g \delta_c \rho_{\text{crit}} R_0^2}{k_B T_g}, \quad (8)$$

where m_p is the proton mass, μ_g is the mean molecular weight of the intra-cluster gas, k_B is the Boltzmann constant, and T_g is the (constant) gas temperature.

Introducing $F_\Phi(\mathbf{r})$:

$$F_\Phi(\mathbf{r}) \equiv \exp \left[-\{\tilde{\Phi}(\mathbf{r}) - \tilde{\Phi}_0\} \right], \quad (9)$$

one can rewrite equation (7) as

$$\rho_g(\mathbf{r}) = \rho_{g0} [F_\Phi(\mathbf{r})]^\kappa. \quad (10)$$

2.2.2. Polytropic gas

The equation of state for the polytropic gas with the polytropic index of γ ($\neq 1$) is given as

$$P_g(\mathbf{r}) = P_{g0} [\rho_g(\mathbf{r})/\rho_{g0}]^\gamma, \quad (11)$$

and its density and temperature profiles in hydrostatic equilibrium are found as ¹

$$\rho_g(\mathbf{r}) = \rho_{g0} \left[1 - \kappa_p \{\tilde{\Phi}(\mathbf{r}) - \tilde{\Phi}_0\} \right]^{\frac{1}{\gamma-1}}, \quad T_g = T_{g0} \left[1 - \kappa_p \{\tilde{\Phi}(\mathbf{r}) - \tilde{\Phi}_0\} \right]. \quad (12)$$

We define a dimensionless polytropic gas constant κ_p as

$$\kappa_p \equiv \frac{\gamma - 1}{\gamma} \frac{4\pi G m_p \mu_g \delta_c \rho_{\text{crit}} R_0^2}{k_B T_{g0}}, \quad (13)$$

and introduce $F_\Phi(\mathbf{r})$:

$$F_\Phi(\mathbf{r}) \equiv 1 - [\tilde{\Phi}(\mathbf{r}) - \tilde{\Phi}_0]. \quad (14)$$

Then one can rewrite equation (12) as

$$\rho_g(\mathbf{r}) = \rho_{g0} [1 - \kappa_p + \kappa_p F_\Phi(\mathbf{r})]^{1/(\gamma-1)}, \quad T_g(\mathbf{r}) = T_{g0} [1 - \kappa_p + \kappa_p F_\Phi(\mathbf{r})]. \quad (15)$$

2.3. Empirical Fitting Formulae for the Gravitational Potential

We have shown in §2.2 that the potential function $F_\Phi(\mathbf{r})$ defines the density and the temperature profiles of intra-cluster gas completely. In general, $F_\Phi(\mathbf{r})$ does not exist in a closed analytic form when the dark matter halos are triaxial ellipsoids. In Paper I, we

¹Note that the definition of Φ_0 in Paper I is different from that given here by a constant offset.

computed $F_\Phi(\mathbf{r})$ analytically with the perturbation theory assuming $e_b^2 \leq e_c^2 \ll 1$, and related the gas iso-density surfaces to that of dark halos; if the halo iso-density surfaces are triaxial ellipsoids with the eccentricities of e_σ ($\sigma = b, c$), then the iso-density surfaces of the intra-cluster gas is also well approximated as triaxial ellipsoids with the eccentricities of ϵ_σ that are related to e_σ by

$$\frac{e_\sigma^2}{e_\sigma^2} = \frac{6(1+u)\ln(1+u) + u^3 - 3u^2 - 6u}{2u^2[(1+u)\ln(1+u) - u]}, \quad (16)$$

where $u = |\mathbf{r}|/R_0$. Note that the right-hand-side of equation (16) are written in terms of the spherical radius u , which results from the fact that we neglected the higher-order terms $O(e_\sigma^4)$ in deriving equation (16) with the help of the perturbation theory. Although equation (16) seems complicated, it is a slowly varying function, and well approximated as a constant in the range of $0 < u < 1$ (see Fig. 3 of Paper I) such that

$$\frac{e_\sigma^2}{e_\sigma^2} \approx 0.7^2. \quad (17)$$

Strictly speaking, equation (17) is valid only in the limit of $e_b^2 \leq e_c^2 \ll 1$ over the range of $0 < u < 1$. To proceed further in a tractable fashion, we extrapolate the result to $e_b^2 \leq e_c^2 \leq 1$ over the whole range of u . In other words, we assume that the iso-density surfaces of the intra-cluster gas are triaxial ellipsoids with the constant eccentricities of ϵ_b, ϵ_c that are related to the halo eccentricities e_b, e_c by equation (17). Actually this turns out to be a good approximation as we show below by comparing it with the numerically computed gas profiles.

This assumptions allows us to write the potential function $F_\Phi(\mathbf{r})$ in terms of the major axis length of the gas iso-density surfaces, ξ , defined as

$$\xi^2 \equiv u_x^2 + \frac{u_y^2}{1 - \epsilon_b^2} + \frac{u_z^2}{1 - \epsilon_c^2} = \frac{1}{R_0^2} \left(x^2 + \frac{y^2}{1 - \epsilon_b^2} + \frac{z^2}{1 - \epsilon_c^2} \right). \quad (18)$$

After some trials and errors, we find that the following empirical functional form fits both equations (9) and (14) very accurately:

$$F_\Phi(\xi) = \left(\frac{1 + \eta \xi^p}{1 + \beta \xi^p} \right)^q, \quad (19)$$

where β, p, q , and η are free parameters. The four free parameters are not constant but expected to depend on the halo eccentricities. We determine their functional forms functional forms according to the following three steps.

1. Compute $F_\Phi(\mathbf{r})$ numerically using equations (3) and (4) for various values of e_b and e_c .

2. Fit those numerical data points to the empirical model (eq. [19]) and obtain the best-fit values of β , p , q , and η using the Levenberg-Marquardt method (Press et al. 1992).
3. Finally model those best-fit parameters as a function of e_b and e_c . In practice, we find that their dependence is written almost entirely in terms of a single variable $\mu \equiv e_b^3 + e_c^3$.

We find that the following polynomials provide simple but accurate fits:

$$\beta = c_{\beta 0} + c_{\beta 1}\mu, \quad (20)$$

$$p = \text{const.}, \quad (21)$$

$$q = c_{q0} + c_{q1}\mu + c_{q2}\mu^2, \quad (22)$$

$$\eta = c_{\eta 0} + c_{\eta 1}\mu. \quad (23)$$

Table 1 lists the best-fit values of the polynomial coefficients. The best-fit values of the constant p is determined to be unity for all cases. Note that we represent the gas profiles in terms of the intrinsic properties of the underlying dark halos by proposing β, p, q, η as functions of μ , which is the essential part of our empirical model.

Figure 1 plots β , q , and η as a function of μ . The filled circles indicate the best-fit values of the parameters, while the solid lines represent their polynomial fits. Note that η is one order-of-magnitude smaller than β for all cases, and thus the term associated with η can be safely neglected except at the outer part of clusters. The accuracy of the fits is illustrated in Figure 2 where $F_\Phi(\xi)$ is plotted against ξ . The solid lines represent the numerical results while the dashed lines correspond to equation (19) with the best-fit coefficients of the polynomials plotted in Fig. 1 and listed in Table 1. Our empirical fitting formulae reproduce the numerical results very well for all cases over a wide range of ξ within a fractional error less than 0.5%.

It is worth mentioning that according to our model the gas density/temperature does not approach zero even at large u . This feature is ascribed to the assumption of the hydrostatic equilibrium itself. In reality, this assumption may be justified only within some radius, e.g., the virial radius of the cluster. In fact, the halo density profiles at those regions are not well approximated by equation (2) because of the presence of substructures, and so on. This problem, however, is not expected to affect our methodology in practice since the X-ray and SZ fluxes from regions beyond the virial radius are usually negligible.

3. PROJECTED SURFACE BRIGHTNESS PROFILES OF INTRA-CLUSTER GAS

Now we are in a position to compute the X-ray and SZ surface brightness profiles of triaxial galaxy clusters using the empirical models for the 3D counterparts (eqs. [10], [15], and [19]) in §2.

Just for comparison, let us recall that the surface brightness profiles of spherical clusters can be readily evaluated as

$$\Sigma(\theta) = \int_{-\infty}^{\infty} L(\sqrt{d_A^2 \theta^2 + z^2}) dz, \quad (24)$$

where θ is the angular radius from the center of the cluster, d_A is the angular diameter distance to the cluster, and L is the emissivity given in terms of ρ_g and T_g such that $L \propto \rho_g^2 T_g^{1/2}$ for bolometric X-ray and $L \propto \rho_g T_g$ for SZ observations, respectively. For the case of triaxial clusters, however, the result is substantially complicated because the 2D projection depends on the relative direction of the line-of-sight of an observer with respect the cluster principal axes. The projection effect of triaxial bodies on the plane of the sky was fully discussed by Stark (1977) and Binney (1985). In what follows we adopt the notation of Binney (1985).

Let (θ, ϕ) be the polar angle of the line-of-sight in the halo principal coordinate system, and let the observer's coordinate system be defined by Cartesian axes (x', y', z') with z' -axis aligned with the line-of-sight direction and x' -axis lying in the (x, y) plane (see Fig. 1 in Oguri, Lee, & Suto 2003). Then the halo principal coordinate system (x, y, z) is related to the observer's coordinate system (x', y', z') by

$$x = -\sin \phi x' - \cos \phi \cos \theta y' + \cos \phi \sin \theta z', \quad (25)$$

$$y = -\cos \phi x' - \sin \phi \cos \theta y' + \sin \phi \sin \theta z', \quad (26)$$

$$z = \sin \theta y' + \cos \theta z'. \quad (27)$$

If we use the major axis length ξ defined in equation (18) to characterize the iso-density surfaces, then the projection of L onto the plane of the sky is written as

$$\Sigma(x', y') \equiv \int_{-\infty}^{\infty} L(\xi) dz' = \frac{1}{\sqrt{f}} \int_{-\infty}^{\infty} L(z''^2 + \lambda^2) dz''^2, \quad (28)$$

where

$$z'' = \sqrt{f} \left(z' + \frac{g}{2f} \right), \quad (29)$$

$$\lambda = \frac{1}{\sqrt{f}}(Ax'^2 + Bx'^2y'^2 + Cy'^2)^{1/2}, \quad (30)$$

$$f = \sin^2 \theta \left(\cos^2 \phi + \frac{\sin^2 \phi}{1 - \epsilon_b^2} \right) + \frac{\cos^2 \theta}{1 - \epsilon_c^2}, \quad (31)$$

$$g = \sin \theta \sin 2\phi \left(\frac{1}{1 - \epsilon_b^2} - 1 \right) x' + \sin 2\theta \left(\frac{1}{1 - \epsilon_c^2} - \cos^2 \phi - \frac{\sin^2 \phi}{1 - \epsilon_b^2} \right) y', \quad (32)$$

$$A = \frac{\cos^2 \theta}{1 - \epsilon_c^2} \left(\sin^2 \phi + \frac{\cos^2 \phi}{1 - \epsilon_b^2} \right) + \frac{\sin^2 \theta}{1 - \epsilon_b^2}, \quad (33)$$

$$B = \cos \theta \sin 2\phi \left(1 - \frac{1}{1 - \epsilon_b^2} \right) \left(1 - \frac{1}{1 - \epsilon_b^2} \right), \quad (34)$$

$$C = \left(\frac{\sin^2 \phi}{1 - \epsilon_b^2} + \cos^2 \phi \right) \frac{1}{1 - \epsilon_c^2}. \quad (35)$$

Hence $\Sigma(x', y') = \Sigma(\lambda)$. In other words, the 2D isophotal curves of triaxial galaxy clusters are concentric and coaxial ellipses if their eccentricities ϵ_σ of *gas* density profiles are constants. As we noted before, however, it is not exactly the case for our model where the eccentricities e_σ of *dark matter* density profiles are constant. Nevertheless this holds in a approximate sense (see eq.[17]).

Let us define a dimensionless surface brightness $\tilde{\Sigma} \equiv \Sigma/\Sigma_0$ where $\Sigma_0 \equiv \Sigma(0)$ and $\tilde{\lambda} = \lambda/R_0$. In the same spirit as for the 3D model (19), we propose the following empirical model for the 2D surface brightness profiles:

$$\tilde{\Sigma}(\tilde{\lambda}; e_b, e_c, \kappa, \kappa_p, \gamma) = \left(\frac{1 + \omega \tilde{\lambda}^s}{1 + \zeta \tilde{\lambda}^s} \right)^t. \quad (36)$$

Now $\tilde{\Sigma}$ depends not only on μ but also on κ (or κ_p), and even on the polytropic index γ for the polytropic case. Thus, we consider the isothermal and polytropic cases separately, and obtain the following empirical fits.

For the isothermal gas, we expand the parameters in quadratic with respect to μ and κ , respectively, as

$$\omega = \sum_{i,j=0}^2 \omega_{ij} \mu^i \kappa^j, \quad (37)$$

$$\zeta = \sum_{i,j=0}^2 \zeta_{ij} \mu^i \kappa^j, \quad (38)$$

$$s = \text{const.}, \quad (39)$$

$$t = \sum_{i,j=0}^2 t_{ij} \mu^i \kappa^j. \quad (40)$$

For the polytropic gas, we fix γ to $\gamma = 1.15$ following Komatsu & Seljak (2001), and expand the parameters in cubic with respect to μ and κ_p :

$$\omega = \sum_{i,j=0}^3 \omega_{ij} \mu^i \kappa_p^j, \quad (41)$$

$$\zeta = \sum_{i,j=0}^3 \zeta_{ij} \mu^i \kappa_p^j, \quad (42)$$

$$s = \text{const.}, \quad (43)$$

$$t = \sum_{i,j=0}^3 t_{ij} \mu^i \kappa_p^j. \quad (44)$$

We determine the best-fit values for ω_{ij} , ζ_{ij} , and t_{ij} using the same method as in §2; first we calculate $\tilde{\Sigma}$ of equation (28) numerically. In practice, we set the bounds of the integration as $\int_{-\infty}^{\infty} L dz' \approx \int_{-z_c}^{z_c} L dz'$ where $z_c = 20R_0$ which is roughly twice the virial radius of galaxy clusters (Makino, Sasaki & Suto 1998). Then we compare the numerical data points of $\tilde{\Sigma}$ with the fitting formula (36), and determine the best-fit values for each point using the Levenberg-Marquardt method. Finally we model the free parameters as polynomials of μ and κ (or κ_p), and determine the best-fit polynomial coefficients.

The best-fit constant values of s is determined to be unity for both the isothermal and polytropic case just like the 3D model. Figures 3 and 4 plot the best-fit parameters as functions of μ for three different values of κ (or κ_p). It is clear from these figures that the polynomial fitting to the free parameters are good approximations for all cases. Tables 2 and 3 list the best-fit coefficients ζ_{ij} , t_{ij} , ω_{ij} for the case of bolometric X-ray and SZ observations respectively.

Figure 5 illustrates the degree of the accuracy of our fitting formulae. The filled squares represent the numerical results while the solid lines correspond to our analytic models with the best-fit polynomials of ζ , t , and ω . We have found that our fits reproduce the numerical results within the fractional error of 20% for all cases in a range of $0 \leq \tilde{\lambda} \leq 10$.

4. DARK HALO RECONSTRUCTION

In the triaxial dark halo model that we adopt here, dark halo reconstruction from the X-ray and SZ cluster observations is basically to determine the shapes (i.e., two eccentricities) and the orientations of the dark halos from the observed surface brightness profiles.

In §4, we provide the analytic fitting model for the X-ray and SZ surface brightness

profiles of galaxy clusters. The models are expressed as a function of the rescaled major axis length of the gas isophotes and characterized by the three free parameters. It turns out that the rescaled major axis length and the three free parameters depend on the eccentricities and the orientation angles of the underlying dark halos, as well as the gas constant. Therefore, we find a way to link the observed 2D surface brightness profiles of galaxy clusters to the underlying dark halos and the intra-cluster gas property. In other words, one may expect to determine the values of (e_b, e_c, θ, ϕ) and (κ, κ_p) by fitting our 2D parameterized models (eqs. [36] – [41]) to the X-ray and SZ cluster data.

In order to test the usefulness of our series of cluster modeling, we test the following reconstruction algorithm for the underlying dark halos against the numerically projected profiles. We first numerically compute $\tilde{\Sigma}$ directly using equations (3)-(28). Then we construct a pixeled map of surface brightness in $N \times N$ grids ($N = 32$ in the present example) corresponding to the linear scale of $-10R_0 \leq x', y' \leq 10R_0$ since $10R_0$ is roughly equal to the cluster virial radius (Jing & Suto 2002). We create several realizations of X-ray and SZ profiles for both isothermal and polytropic with $\gamma = 1.15$, and for various different values of e_b, e_c, θ, ϕ .

Our reconstruction algorithm proceeds as follows;

- It is assumed that it can be *priori* determined whether the intra-cluster gas is isothermal or polytropic.
- At each pixel point, say, (x'_i, y'_j) , build the model $\tilde{\Sigma}^{\text{th}}(x'_i, y'_j)$ using equation (36). The model is characterized by the five free parameters $e_b, e_c, \theta, \phi, \kappa$ (or κ_p) at each point.
- Fit $\tilde{\Sigma}^{\text{th}}$ to the observed surface brightness density profiles $\tilde{\Sigma}^{\text{obs}}$, and calculate the χ^2 :

$$\chi^2 = \sum_{i,j=1}^N \frac{[\tilde{\Sigma}^{\text{th}}(x'_i, y'_j) - \tilde{\Sigma}^{\text{obs}}(x'_i, y'_j)]^2}{\sigma_{ij}^2}, \quad (45)$$

where σ_{ij} denotes the observational error at each pixel point (x'_i, y'_j) . Those systematic/random errors should depend on specific observation conditions and thus are not easy to estimate a priori. Thus in the following numerical tests, we simply assume that σ_{ij} is constant and independent of i and j .

- Determine the best-fit values of $e_b, e_c, \theta, \phi, \kappa$ (or κ_p) through the χ^2 minimization.

From the numerical testing, it turns out that the above algorithm works quite well in reconstructing the halo eccentricities within the fractional error of 20% as far as the halo eccentricities are not so small ($e_b, e_c > 0.3$). The algorithm also works in reconstructing the

orientation angles but with relatively larger fractional errors than those of the eccentricities. We show examples of our numerical reconstruction results in Figures 6 and 7 for the following cases of the halo eccentricities and orientation angles: $(e_b, e_c) = (0.4, 0.7), (0.5, 0.6)$, and $(0.6, 0.8)$; $(\theta, \phi) = (15, -75), (45, -45), (75, -15)$ in units of degree.

Figure 6 plots the fractional error of the reconstructed eccentricities versus their input values for three different cases of the orientation angles. The left three panels are for e_b , and the right three panels for e_c . The top two panels correspond to the case of $\theta = 15^\circ$ and $\phi = -75^\circ$, the middle two panels to the case of $\theta = 45^\circ$ and $\phi = -45^\circ$, and the bottom three panels to the case of $\theta = 75^\circ$ and $\phi = -15^\circ$. For almost all cases, the fractional errors fall within 20%.

Figure 7 plots the fractional error of the reconstructed orientation angles versus the original orientation angles from three different cases for the eccentricities. The left three panels are for θ , and the right three panels for ϕ . The top two panels correspond to the case of $e_b = 0.4$ and $e_c = 0.7$, the middle two panels to the case of $e_b = 0.5$ and $e_c = 0.6$, and the bottom three panels to the case of $e_b = 0.6$ and $e_c = 0.8$. For most cases, the fractional errors fall within 20%. However, for a few cases, the fractional errors are larger than 50%, indicating that the angle reconstruction is not so stable compared with the eccentricity reconstruction.

5. DISCUSSIONS AND CONCLUSIONS

We have provided an analytic model for the X-ray and SZ surface brightness density profiles of galaxy clusters. Our model is based on the assumptions that the intra-cluster gas is in hydrostatic equilibrium within the gravitational potential generated by a triaxial dark matter halo, and that the 2D projected isophotes of galaxy clusters are well approximated as coaxial and concentric ellipses. The derived sets of empirical fitting formulae directly reflect the information of the 3D structure of the triaxial dark matter halos; the two eccentricities of the triaxial dark halos and the orientation angles of the halo principal axes in the observers frame. Therefore, one may expect that our model can be used in reconstructing the 3D structure of the underlying dark halos via determining the best-fit values of those parameters.

We have proposed a numerical algorithm based on our analytic model to determine the halo eccentricities and orientation angles from the observed X-ray and SZ surface brightness density profiles of galaxy clusters, and tested the reconstruction algorithm against simple numerical model profiles. We found that the algorithm can reconstruct the halo eccentricities fairly accurately as far as the halo eccentricities are greater than 0.3. However, it also turns out that the reconstruction of the halo orientation angles are not always accurate, showing

large scatters.

Empirical as our analytic model for the intra-cluster gas is, it is worth mentioning that our model has been derived from the first principles, and thus express the intra-cluster gas surface brightness profiles in terms of the intrinsic properties of the underlying dark halos, which is the essential and unique part of our model. Our reconstruction algorithm is general in a sense that it does not assume the axis symmetry of triaxial dark halos, which all previous approaches are based on, and that it does not require any further information about the galaxy cluster such as weak gravitational lensing data. We plan to directly apply the current reconstruction algorithm to real observational data, and wish to report the result elsewhere.

We thank Masamune Oguri for useful discussions. J. L. acknowledges gratefully the research grant of the JSPS (Japan Society of Promotion of Science) fellowship. This research was supported in part by the Grant-in-Aid for Scientific Research of JSPS (12640231).

REFERENCES

Binney, J. 1985, MNRAS, 212, 767

Binney, J., & Tremaine, S. 1987, Galactic Dynamics (Princeton: Princeton Univ. Press)

Binney, J. J., Davies, R. L., & Illingworth, G. D. 1990, ApJ, 31, 78 Birkinshaw, M. 1999, Phys. Rep., 310, 97

Dehnen, W., & Gerhard, O. E. 1993, MNRAS, 261, 311

Dore, O., Bouchet, F. R., Mellier, Y., & Teyssier, R. 2001, A&A, 375, 14

Fabricant D., Rybicki, G. & Gorenstein, P. 1984, ApJ, 286, 186

Fox, D. C., & Pen, U. L. 2002, ApJ, 574, 38

Gerhard, O., & Binney, J. 1996, MNRAS, 279, 993

Fukushige, T., & Makino, J. 1997, ApJ, 477, L9

Jing, Y. P., & Suto, Y. 2000, ApJ, 529, L69

Jing, Y. P., & Suto, Y. 2002, ApJ, 574, 538

Komatsu, E. et al. 2001, PASJ, 53, 57

Komatsu, E. & Seljak, U. 2001, MNRAS, 327, 1353

Lee, J. & Suto, Y. 2003, ApJ, 585, 151

Lucy, L. B., 1974, AJ, 79, 745

Makino, N., & Sasaki, S., & Suto, Y. 1998, ApJ, 497, 555

Moore, B., & Governato, F., Quinn, T., & Stadel, J., Lake, G. 1998, ApJ, 499, L5

Navarro, J.F., Frenk, C.S., & White, S. D. M. 1996, ApJ, 462, 563

Navarro, J.F., Frenk, C.S., & White, S. D. M. 1997, ApJ, 490, 493

Oguri, M., Lee, J., & Suto, Y. 2003, ApJ, submitted

Press, W. H., Teukolsky, S. A., Vetterling, W. T., & Flannery, B. P. 1992, Numerical Recipes in Fortran, (Cambridge: Cambridge Univ. Press)2nd ed.

Reblinsky, K. 2000, A&A, 364, 377

Stark, A. A. 1977, *ApJ*, 213, 368

Suto, Y., Sasaki, S., & Makino, N. 1998, *ApJ*, 509, 544

Yoshikawa, K., & Suto, Y. 1999, *ApJ*, 513, 549

Yoshikawa, K., Taruya, A. & Suto, Y. 2001, *ApJ*, 558, 520

Zaroubi, S., Squires, G., Hoffman, Y., & Silk, J. 1998, *ApJ*, 500, L87

Zaroubi, S., Squires, G., Gasperis, Evrard, A. E., Hoffman, Y. Y., & Silk, J. 1998, *ApJ*, 500, L87

Table 1: Best-fit polynomial coefficients for the profiles of halo gravitational potentials

(μ)	Isothermal			Polytropic		
	β	q	η	β	q	η
0	1.329	0.426	0.146	0.780	0.617	-0.002
1	0.118	-0.246	0.036	0.470	-0.487	0.133
2	-0.010	0.044	0.009	-0.087	0.136	-0.013

Table 2: Best-fit polynomial coefficients for the profiles of the surface brightness in the isothermal case.

$(\mu \ \kappa)$	X-ray			SZ		
	ζ	t	ω	ζ	t	ω
0 0	3.228	-1.127	-0.121	-3.140	0.447	0.014
0 1	-0.206	0.368	0.044	1.133	-0.087	-0.005
0 2	0.008	0.026	-0.002	-0.058	0.018	0.001
1 0	-0.850	3.749	-0.010	3.874	-0.298	0.056
1 1	1.354	-1.314	-0.032	-1.786	0.101	-0.015
1 2	-0.126	0.037	0.003	0.166	-0.027	0.000
2 0	-12.23	-2.184	0.158	0.297	-0.003	-0.042
2 1	2.253	0.840	-0.025	0.342	-0.015	0.014
2 2	-0.082	-0.044	0.000	-0.064	0.011	-0.001

Table 3: Best-fit polynomial coefficients for the profiles of the surface brightness in the polytropic case with $\gamma = 1.15$.

$(\mu \ \kappa_p)$	X-ray			SZ		
	ζ	t	ω	ζ	t	ω
0 0	2.261	-0.943	-0.257	-3.667	2.542	0.101
0 1	-2.689	0.753	1.027	16.32	-7.786	-0.508
0 2	1.609	6.874	-1.096	-19.30	7.135	0.885
0 3	-0.526	1.328	0.323	7.156	2.345	-0.483
1 0	-0.049	30.48	0.371	-3.390	-19.12	0.424
1 1	13.86	-112.8	-2.301	-0.685	77.61	-1.296
1 2	-27.91	123.3	3.722	19.05	-100.4	0.845
1 3	14.97	-54.25	-1.647	-14.10	32.19	0.145
2 0	-61.22	-67.95	0.836	36.73	34.75	-1.279
2 1	197.2	268.9	-1.902	-125.8	-147.3	4.857
2 2	-199.1	-331.6	0.485	129.1	201.9	-5.537
2 3	63.66	139.9	0.440	-39.35	-79.83	1.742
3 0	56.23	38.90	-0.874	-28.90	-18.29	0.806
3 1	-201.0	-157.9	2.863	107.2	78.73	-3.186
3 2	227.3	202.3	-2.703	-123.9	-110.4	3.918
3 3	-82.35	-86.20	0.743	44.58	46.37	-1.428

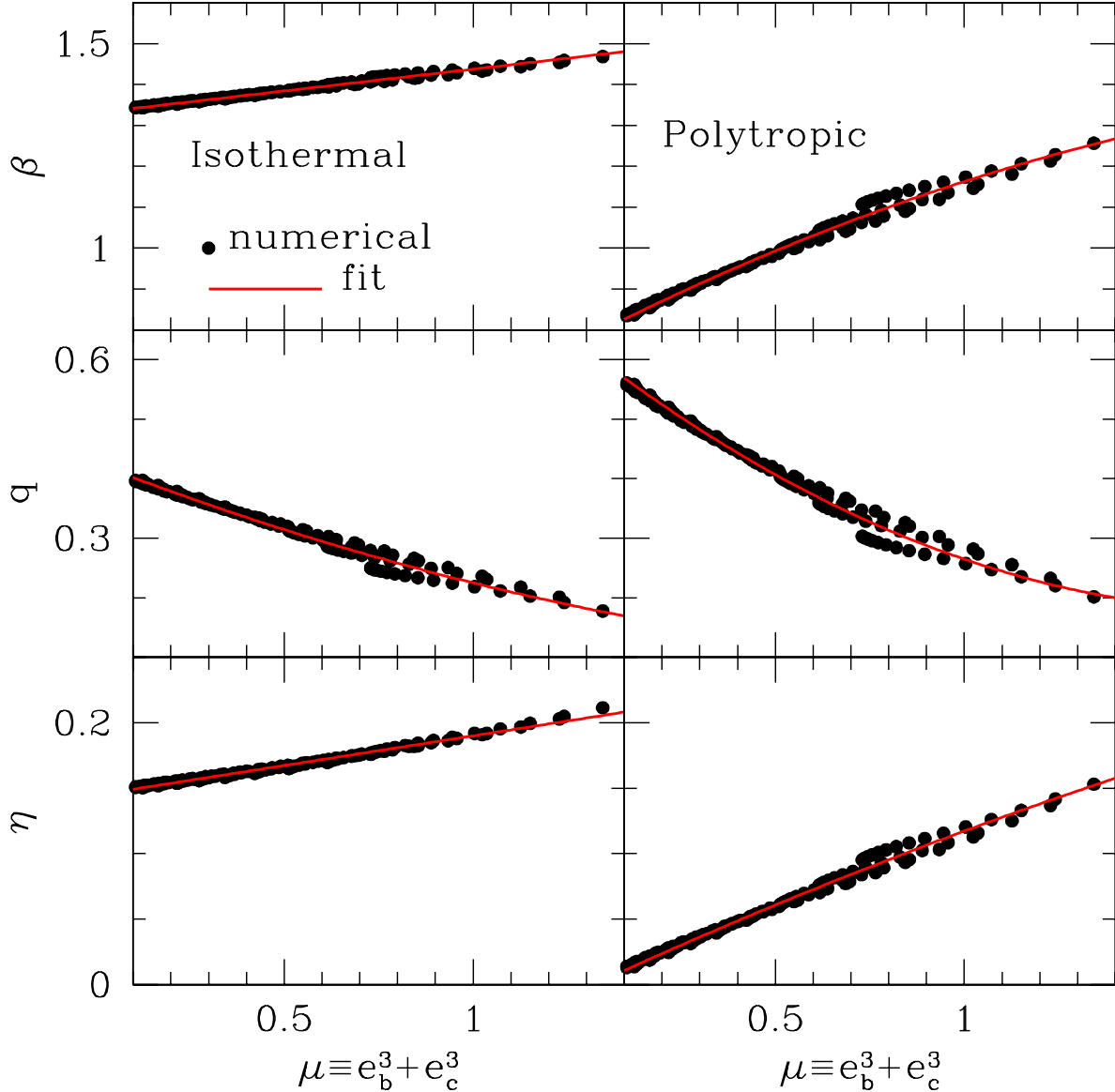


Fig. 1.— Parameters describing our empirical model of the halo potential profile (eq.[19]) as a function of the halo eccentricities ($\mu \equiv e_b^3 + e_c^3$). The filled circles represent the best-fit values to the numerical results at each μ , and the solid curves show the corresponding polynomial fitting curves. The intra-cluster gas is assumed to be isothermal (*Left*) and polytropic (*Right*).

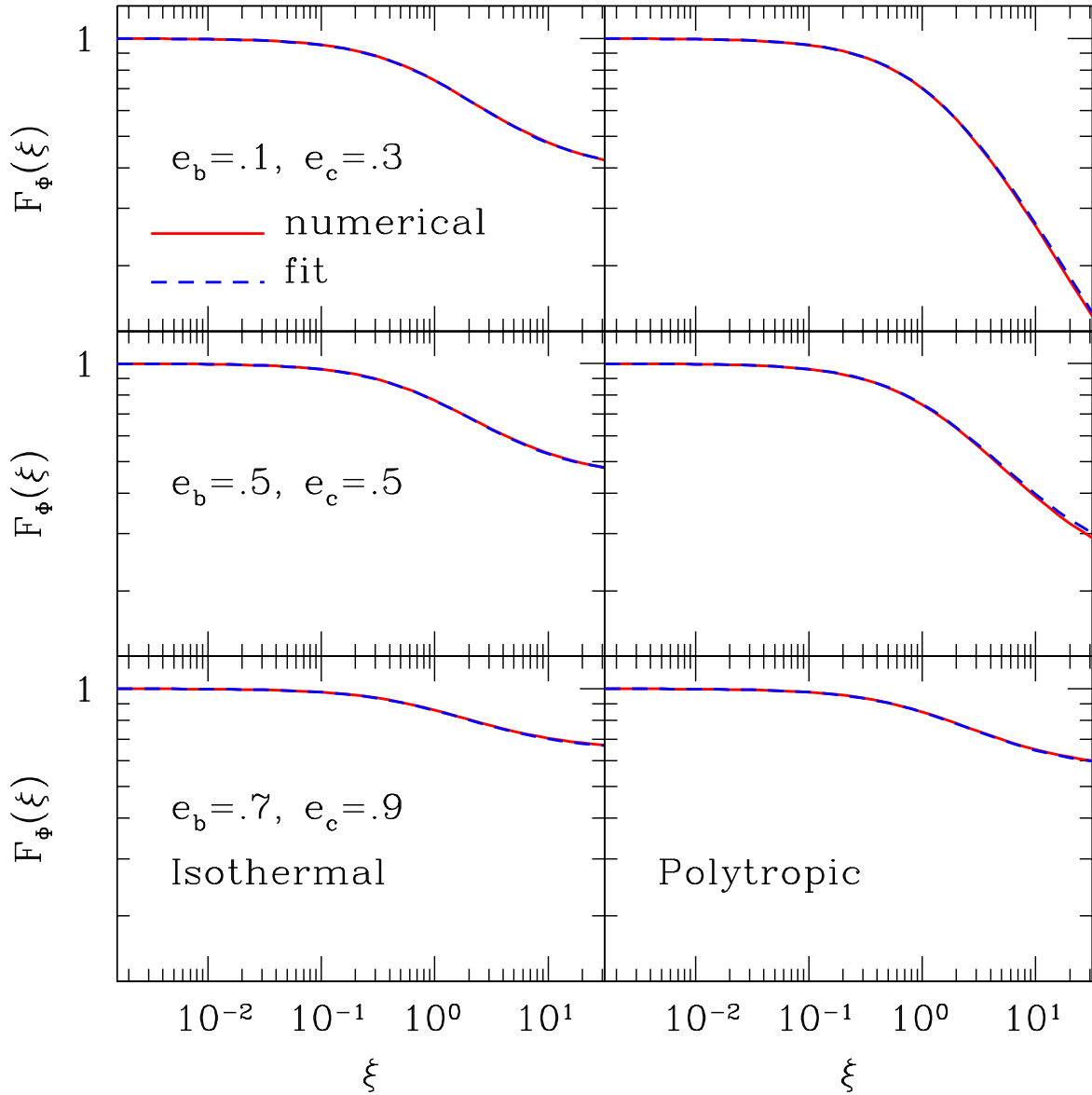


Fig. 2.— Profiles of gravitational potentials of dark halos. Solid and dashed lines indicate the results of the direct numerical integration and our empirical fitting model, respectively. The intra-cluster gas is assumed to be isothermal (*Left*) and polytropic (*Right*). The eccentricities of the underlying dark halos are *Top*: $e_b = 0.1$ and $e_c = 0.3$, *Middle*: $e_b = 0.1$ and $e_c = 0.7$, *Bottom*: $e_b = 0.7$ and $e_c = 0.9$.

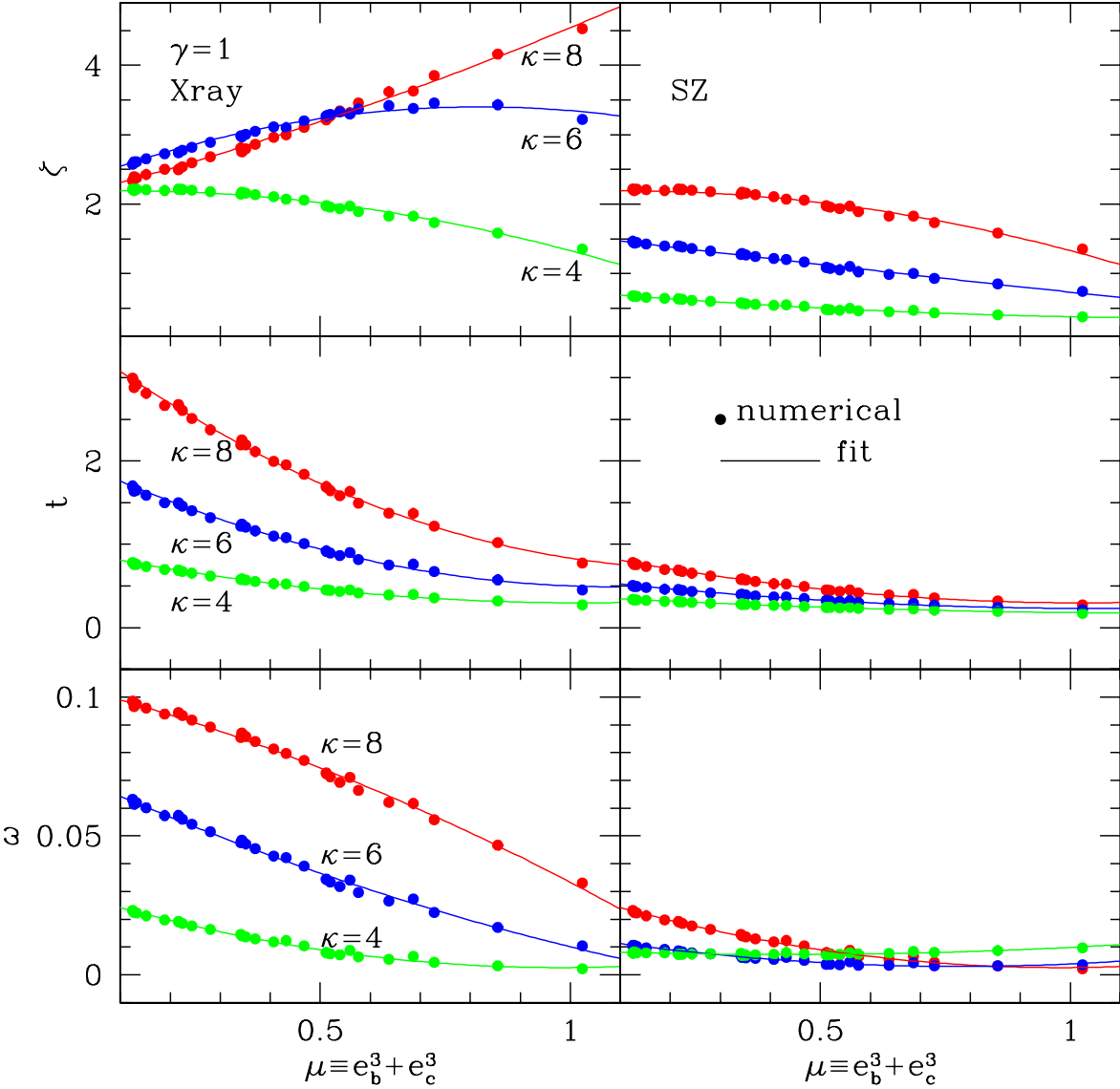


Fig. 3.— Parameters describing our empirical model of the surface brightness profile (eq.[36]) as a function of μ for the isothermal case. The filled circles represent the best-fit values to the numerical results at each μ , and the solid curves show the corresponding polynomial fitting curves. *Left:* X-ray. *Right:* SZ.

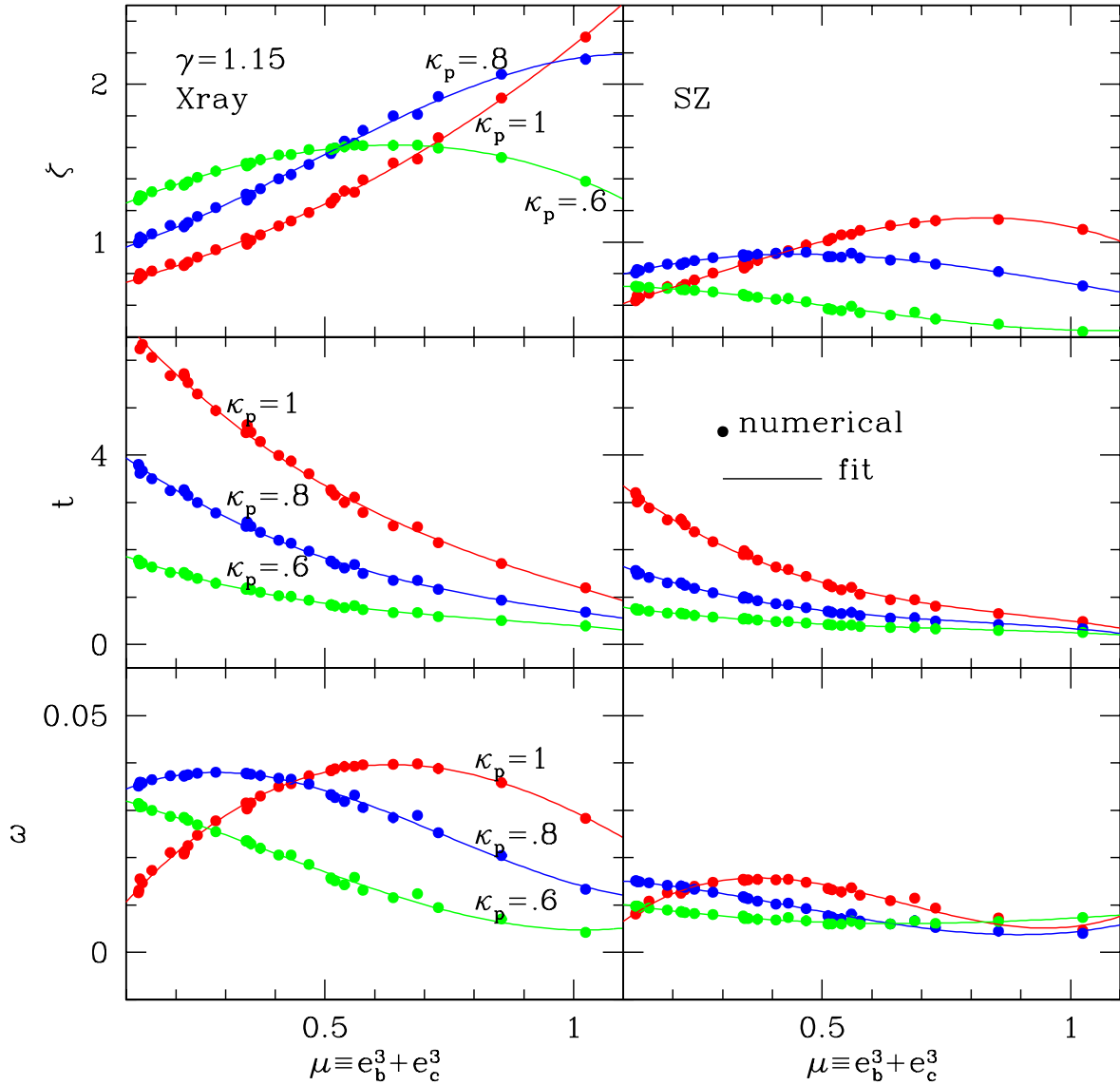


Fig. 4.— Same as Figure 3 but for the polytropic case.

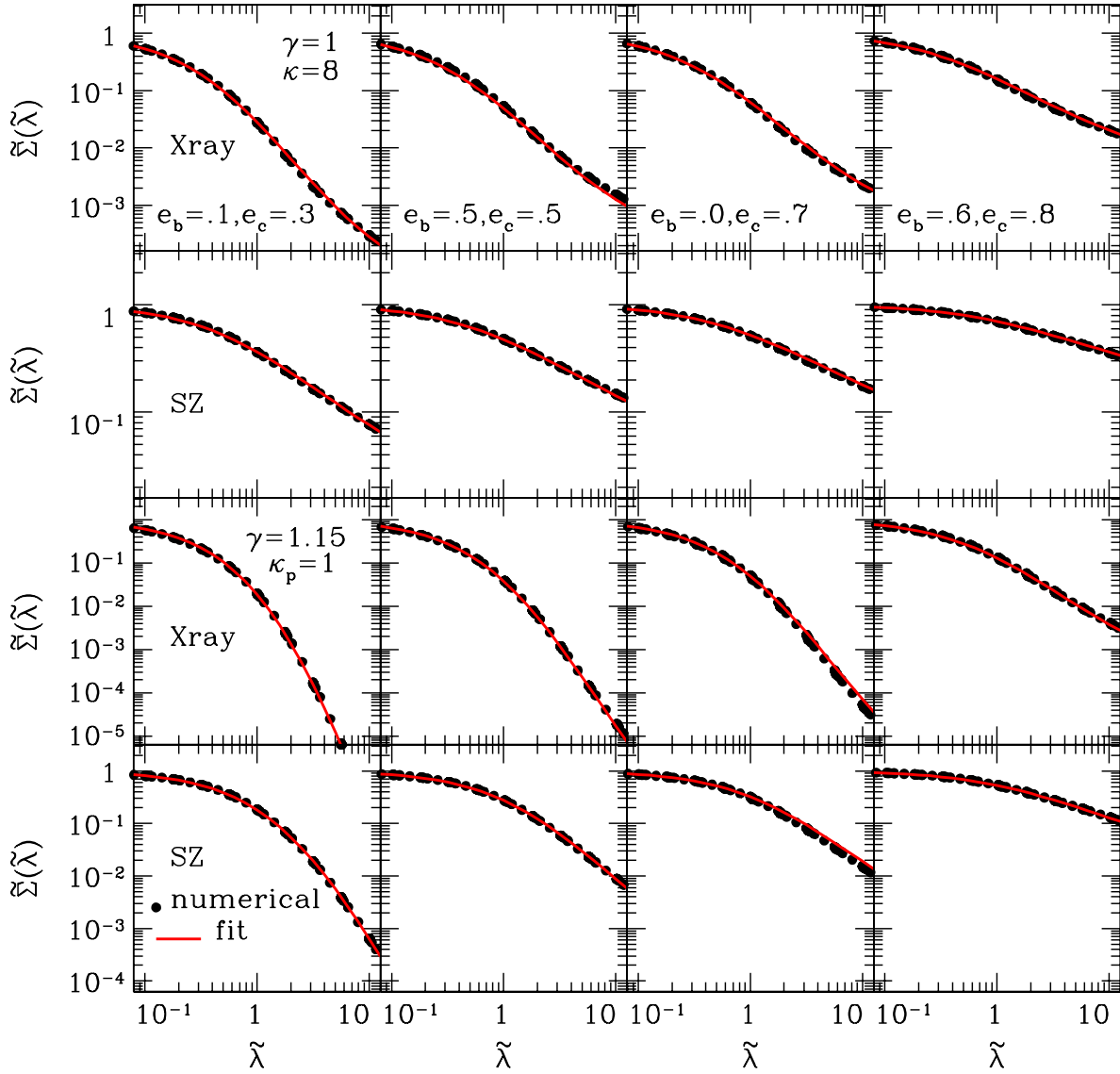


Fig. 5.— Profiles of the cluster surface brightness. The filled circles are computed numerically, while our fitting models are shown in solid lines. From left to right panels, we adopt the underlying halo eccentricities of $(e_b, e_c) = (0.1, 0.3), (0.5, 0.5), (0.0, 0.7)$ and $(0.6, 0.8)$. From top to bottom panels, we show the cases of isothermal X-ray ($\kappa = 8$), isothermal SZ ($\kappa = 8$), polytropic X-ray ($\gamma = 1.15$ and $\kappa_p = 1$), and polytropic SZ ($\gamma = 1.15$ and $\kappa_p = 1$) observations.

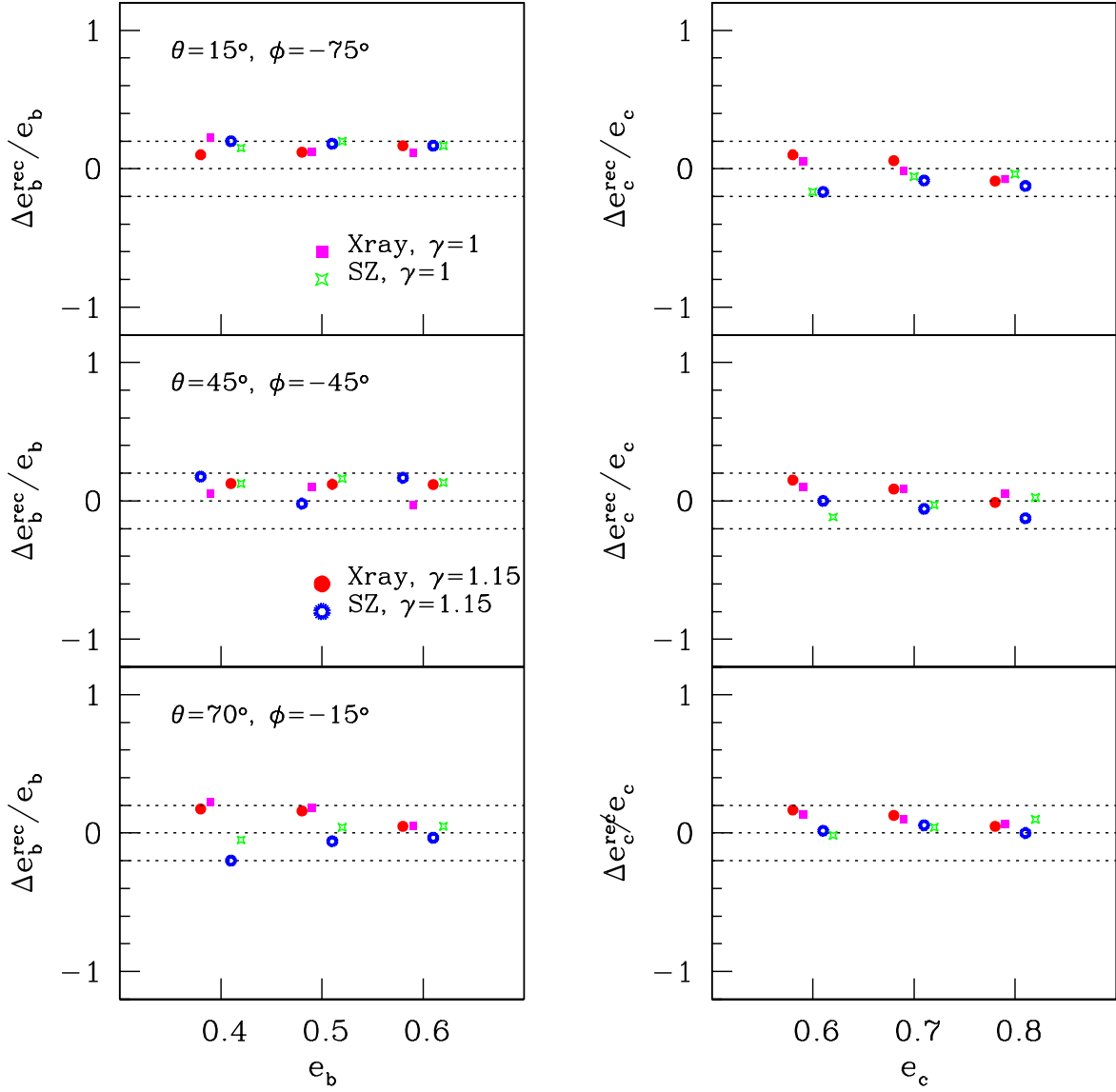


Fig. 6.— Fractional errors of the reconstructed halo eccentricities. Filled squares, open squares, filled circles, and open circles correspond to the cases of isothermal X-ray, isothermal SZ, polytropic X-ray, and polytropic SZ, respectively. We adopt the orientation angles of the line-of-sight with respect to the cluster in the halo principal frame as $(\theta, \phi) = (15^\circ, -75^\circ)$, $(45^\circ, -45^\circ)$, and $(75^\circ, -15^\circ)$ from top to bottom panels.

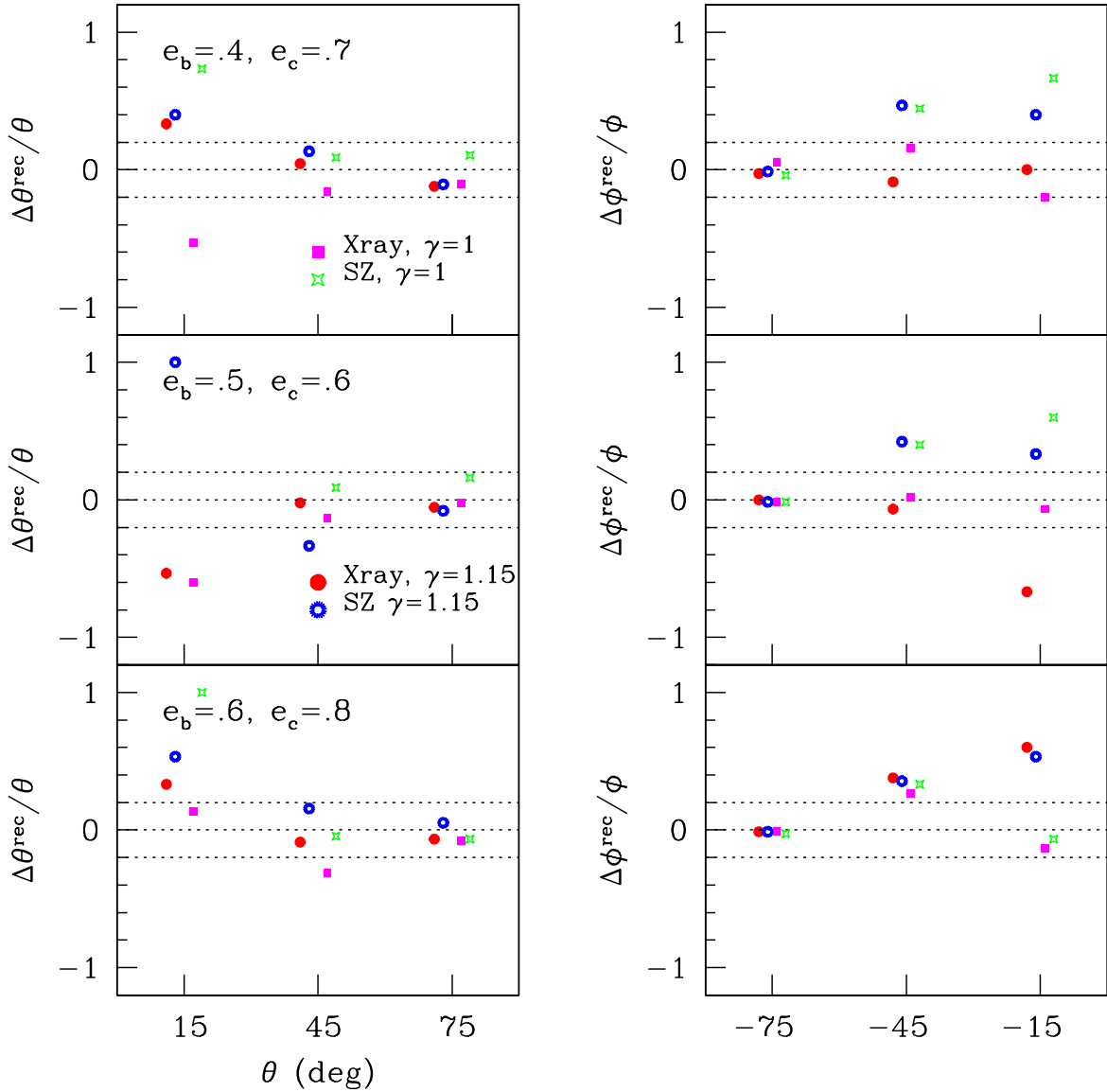


Fig. 7.— Fractional errors of the reconstructed orientation angles. Filled squares, open squares, filled circles, and open circles correspond to the cases of isothermal X-ray, isothermal SZ, polytropic X-ray, and polytropic SZ, respectively. We adopt the halo eccentricities of $(e_b, e_c) = (0.4, 0.7), (0.5, 0.6)$, and $(0.6, 0.8)$ from top to bottom panels.